Journal of Zhejiang University-SCIENCE A (Applied Physics & Engineering)
ISSN 1673-565X (Print); ISSN 1862-1775 (Online)
www.zju.edu.cn/jzus; www.springerlink.com
E-mail: jzus@zju.edu.cn

Driving force and structural strength evaluation of a flexible mechanical system with a hydrostatic skeleton

Daisuke MARUYAMA, Hitoshi KIMURA, Michihiko KOSEKI, Norio INOU[†‡]

(*Department of Mechanical and Control Engineering, Tokyo Institute of Technology, Tokyo 152-8550, Japan*)

[†]E-mail: inou@mech.titech.ac.jp

Received Jan. 19, 2010; Revision accepted Jan. 19, 2010; Crosschecked Jan. 27, 2010

Abstract: The purpose of this study was to build a flexible mechanical system with a hydrostatic skeleton. The main components of this system are two type flexible bags. One is a structural bag with constant inner pressure. The other is an actuator bag with controlled inner pressure. To design the system, it was necessary to estimate both structural deformation and driving force. Numerical analysis of flexible bags, however, is difficult because of large nonlinear deformation. This study analyzed structural strength and driving force of flexible bags with the nonlinear finite element analysis (FEA) software ABAQUS. The stress concentration dependency on the bag shape is described and the driving force is calculated to include the large deformation. From the analytical results, this study derives an empirical equation of driving force. The validity of the equation was confirmed by condition-changed analyses and experimental results.

Key words: Flexible mechanical system, Hydrostatic skeleton, Design method, Nonlinear finite element analysis (FEA)
doi:10.1631/jzus.A000030 **Document code:** A **CLC number:** O35

1 Introduction

1.1 Background

A flexible mechanism with soft materials has several advantages. For example, the flexible parts greatly decrease impact accident risk. A soft gripper can readily grasp a fragile object in a controlled fashion. Terrain adaptive deformation is also a performance advantage of flexible mechanisms, being particularly useful, for example, for utilizing robots in narrow spaces (Kimura *et al*., 2006).

This study deals with a new flexible mechanical system with a hydrostatic driving mechanism. Flexible bags are the main components of this mechanism. The bags are classified into a structural part and an actuator part. This division of roles improves the driving efficiency because only actuator parts consume driving fluid. Conventional flexible mechanisms (Suzumori and Abe, 1993; Suzumori *et al*., 1997; Hayakawa and Pandian, 2005) do not divide these roles, yet, a certain amount of pressure fluid is necessary for driving. High portability is also an advantage of the proposed mechanism. Since the mechanism does not use rigid structural parts, it can be compactly folded when the bags are depressurized.

With flexible mechanisms, however, there is the difficulty of large deformation, which cannot be neglected in design. If the behavior of the flexible bags is unknown, it is also impossible to estimate their driving force. As well, prediction of large deformation of flexible objects is generally quite difficult because of nonlinearity. Recently, with the development of computer technology, it has become possible to calculate deformation with nonlinear finite element analysis (FEA). With the capability of numerical analysis a mechanism can be designed with quantitative estimation. There are several previous studies of flexible models. Kozulin and Skripnyak (2004) discussed the strength of curved pipeline. Pamplona *et al.* (2006) specifically reported the stretching force in a longitudinal direction.

This paper deals with both structural strength

[‡] Corresponding author

and driving force using the nonlinear FEA software ABAQUS. With regard to structural strength, stress concentration of flexible bags with several shapes is described. The optimum fillet radius is also estimated. In terms of driving force, the torque of actuator parts is calculated from the reaction force at analytically fixed points. This torque analysis is particularly difficult because the actuator part is greatly deformed during force generation. An empirical equation of the torque is derived from the analysis. The equation is verified by condition-changed analyses and experimental results.

1.2 Proposed mechanical system

Fig. 1 shows the proposed mechanical system. The system consists of a hydrostatic skeleton made of thin soft materials with two type flexible bags. One acts as the structural part with constant inner pressure. The other is an actuator with controlled inner pressure to generate the driving force through joint torque. A simple example of a hydrostatic skeleton is shown in Fig. 2. The skeleton can transform its shape under conditions of low inner pressure. When a flexible bag pressurizes, it becomes stiffer, like an inflated balloon, generating the structural formation.

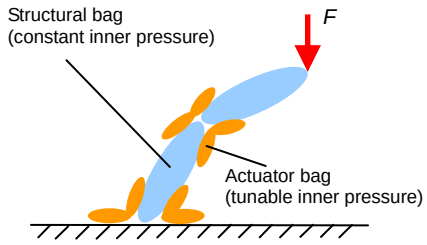

Fig. 1 A basic concept of the proposed mechanical system

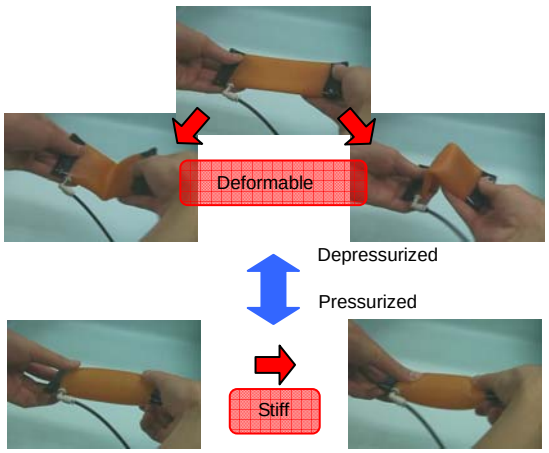

Fig. 2 Deformation of a hydrostatic skeleton with changes in pressure

A pressurized flexible bag has a specific shape. If the inner pressure increases, the shape recovery force increases. This shape recovery force is then used as joint torque. When a hydrostatic skeleton consists of flexible materials like rubber, lightweight and flexible mechanisms can be developed.

A basic configuration of this system is a series of structural bags and actuator bags arranged at the joints. Conceivable applications of the system are robotic arms and robotic hands as illustrated in Fig. 3a. The intermediate joint has two active degrees of freedom (DOFs) with three or more actuator bags as shown in Fig. 3b. Fig. 4 shows our prototype robotic arm. This prototype uses three structural bags and four actuator bags at each joint. The shape of the structural bag is cylindrical with two cones at either end. The diameter of the bag is 100 mm. The length of the cylinder is 200 mm, and the height of the cone is 50 mm. The actuator bags are 180 mm in length and 40 mm in width. Both bags are made of urethane rubber sheets of 0.3 mm thickness. The arm can perform more than a single direction bent form, but also an “S-shape” form. This “S-shape” is not readily accomplished by conventional lightweight arms.

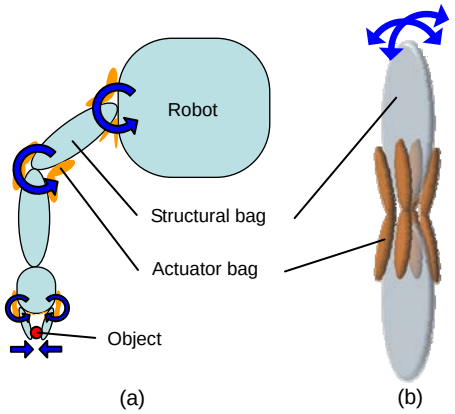

Fig. 3 Applications of the proposed system. (a) A robotic arm with a hand; (b) A 2-DOF joint

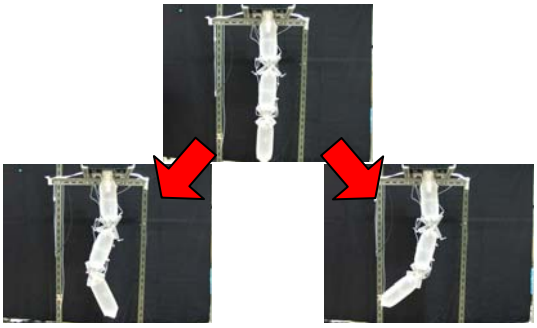

Fig. 4 A prototype of a robotic arm

2 Strength evaluation for structural bags

In this section, as an aspect of strength evaluation, stress concentration is discussed comparing several basic shapes of structural bags.

2.1 Evaluation method

In this study, a structural bag is made of urethane rubber sheets with thermal compression bonds. This method can produce various shapes. Urethane rubber has material nonlinearity, however, because of its flexibility. To obtain the material properties, uniaxial tension tests are performed. The results are indicated in Fig. 5. The material property of biaxial tension states is approximately 1.4 times larger than uniaxial tension states. Material modulus of the third-order Ogden model (Ogden, 1972; 1997) is determined by these two material properties. This model is used widely in nonlinear FEA of rubber materials. The static stress becomes analyzable due to the material modulus. The analytical models are made of urethane rubber sheets with a thickness of 1.1 mm using shell elements, and 0.005 MPa inner pressures are provided. Boundary conditions are given so as to have no effect on model deformation. This analysis uses the implicit method with ABAQUS. All subsequent analyses are performed with 1.0 mm mesh size. The element number depends on the mesh size, and it is about 10000–30000 in each FEA model.

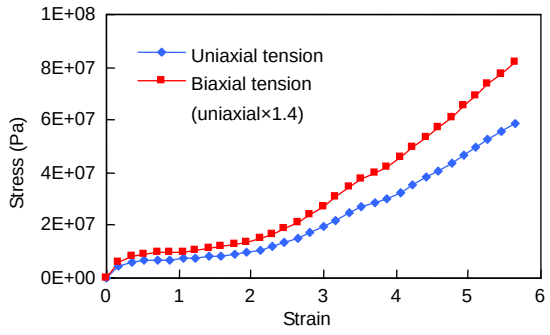

Fig. 5 Material characteristics of uniaxial and biaxial tensions

2.2 Stress concentration in convex shape

A round shape and a square shape were analyzed. The round shape is 100 mm in diameter, and the square shape is 100 mm in side dimension. The analytical results are shown in Fig. 6. The stress concentration of the round shape occurs uniformly on the outer circumference. On the other hand, the stress concentration of the square shape occurs at the four corners. The maximum stress is larger than that of the round shape in the same scale. From these results, the round shape seems to be suitable for a structural bag.

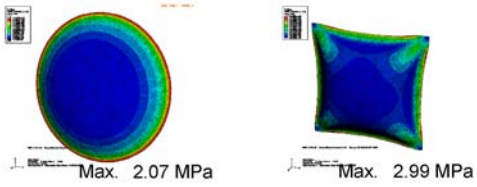

Fig. 6 Analytical results of (a) a round shape and (b) a square shape

Next, elliptical shapes and rectangular shapes are analyzed. The elliptical shapes are set at 50 mm in long radius and 40, 30 and 20 mm in short radius. Similarly, the rectangular shapes are set at 100 mm on the long side and 80, 60 and 40 mm on the narrow side. The analytical results are illustrated in Figs. 7 and 8.

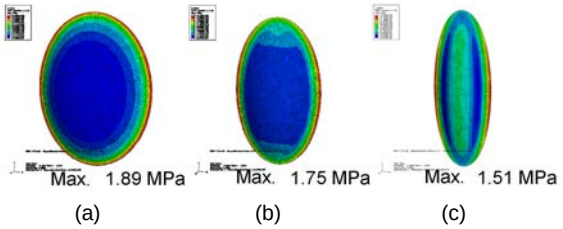

Fig. 7 Analytical results of elliptical shapes. (a) 40 mm; (b) 30 mm; (c) 20 mm in short radius

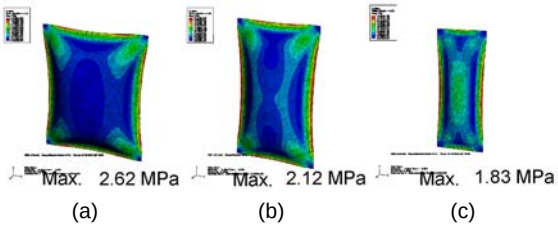

Fig. 8 Analytical results of rectangular shapes. (a) 80 mm; (b) 60 mm; (c) 40 mm on the narrow side

These results show that the maximum stress of 20 mm in short radius is the minimum value of these models. On the other hand, in the rectangular shapes, the maximum stress of 40 mm along the narrow side is smaller than those of the other rectangular shapes. In addition, the stress concentration of the rectangular shapes appears in the center as the narrow side becomes shorter. The maximum values and the

distribution of the stress suggest that a highly elliptical shape is the most suitable convex shape in terms of stress concentration.

2.3 Stress concentration in concave shape

Cross-shaped models were also analyzed for the evaluation of a concave shape. The concave shape is fillet. The branch length of the cross is determined far enough along the width so that deformation of the branch end does not affect the deformation of fillets. The relation between width (W) and fillet radius (R) was calculated. The analytical results with 30 mm in width and 10, 20 and 30 mm in fillet radius are shown in Fig. 9.

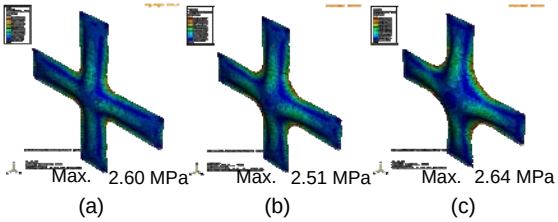

Fig. 9 Analytical results of cross shapes with 30 mm in width. (a) R=10 mm; (b) R=20 mm; (c) R=30 mm

The 20-mm radius fillet model has the least maximum stress. This suggests that there is an optimum fillet radius against the width of the branch. Fig. 10 displays the relation between the optimum fillet radius and the width of the branch, the dependency linearly approximated by the least square method. The optimum fillet radius is about 0.7 times the width of the branch.

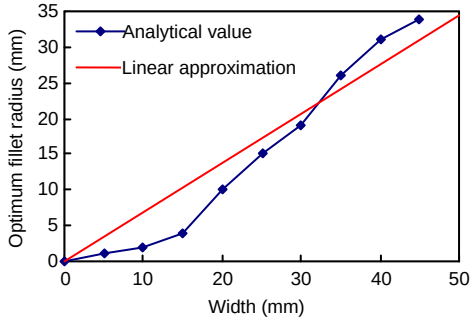

Fig. 10 Optimum fillet radius versus cross shape width

T-shaped models with widths of 30 and 50 mm also reveal similar results. The optimum fillet radius for a cross shape is applicable to a T-shape, and this observation contributes to the optimum design of a structural bag.

3 Evaluation of driving force for actuator bags

The driving force is generated through the torque of an inflated actuator bag. For torque estimation, large deformation of actuator bags was analyzed by nonlinear FEA. Based on the analytical results, an empirical equation of the torque was obtained by polynomial approximation.

3.1 Simplified model

In our former study, a simplified model for torque was discussed (Kimura *et al*., 2006). Based on the equilibrium of work volume, the relation between torque T and the volume change ΔV is represented by the following equation:

$$T\Delta\theta = p\Delta V, \tag{1}$$

where $\Delta\theta$ is the angle change, and p is the inner pressure. The model is built on a supposition that the cross section of the bending part is an elliptical shape. Measuring the length of the elliptical part, ΔV can be calculated. This estimation generally indicates the similar tendency of experimental torque. In the extremes of small and large θ, however, the model cannot follow the experimental torque. To obtain greater accuracy, a new model is adopted in this study.

3.2 Evaluation based on nonlinear FEA

Torque estimation is more difficult than structural bag analysis due to the large deformation with thin materials. To deal with this, the explicit FEA with membrane elements is used for the torque analysis. This analysis also uses the software ABAQUS.

The FEA model has a bent shape at the midpoint, and the torque is generated by inflation of the model. The FEA needs only one step to obtain the inflated state. The time length of this step is 20 s. The inner pressure increases in the initial 10 s. The longitudinal length (L) is set constant, at 200 mm. All subsequent analyses are performed with 2.0 mm mesh size. The element number depends on the mesh size, and it is about 10000 in each FEA model.

A boundary condition of the model is illustrated in Fig. 11. The torque is calculated from the reaction force at the side edges of the model. The position of the reaction force is located at the quarter length of the side edge. It is denoted by arrows in Fig. 11.

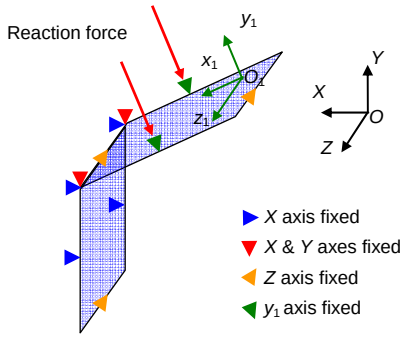

Fig. 11 Boundary condition of the model

Because of numerical oscillation, a filtering approach is used to determine the reaction force. We confirmed that values from analytical results with filtering were equal to the values of long time length analyses without filtering. The deformations at several bending angles are illustrated in Fig. 12.

In terms of bending angle θ, the torque is calculated from 10° to 160°. At first, torque dependency on inner pressure (P) is calculated under a constant width (W), 40 mm. Inner pressure is then changed from 0.005 MPa to 0.04 MPa. Fig. 13a shows the relation between the torque and the angle, and the torque dependency on the inner pressure is plotted in Fig. 13b.

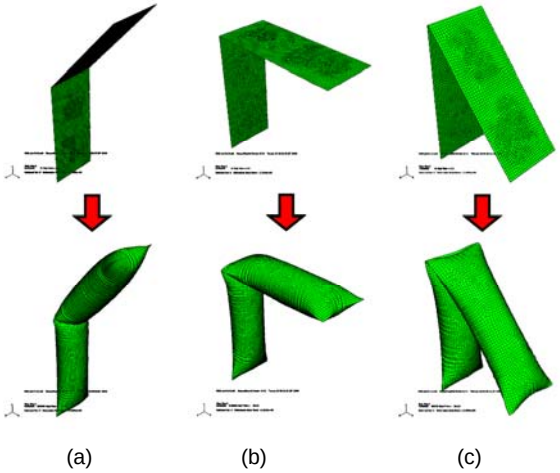

Fig. 12 Deformation of the analyzed models. (a) θ=40°; (b) θ=90°; (c) θ=140°

The torque proportionally increases with inner pressure under constant bending angle and width. From this observation, we obtain a proportional factor k_1 between the torque and inner pressure, where k_1 is a dimensionless value because k_1 is described by the after-mentioned Eq. (3).

k_1 of each bending angle is indicated in Fig. 14. This result is obtained from linearized slopes in Fig. 13b divided by a criteria torque. The criteria torque is calculated under 40 mm width, 200 mm length and 0.02 MPa inner pressure. Since k_1 values are nearly constant, we determine the proportional factor k_1 as 5.2×10^{-5}.

Next, torque dependency on width is analyzed at constant inner pressure, 0.02 MPa. Width is changed

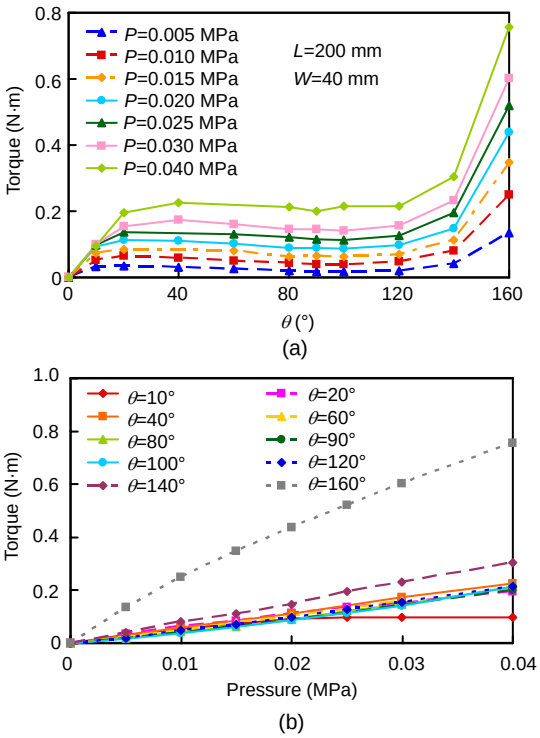

Fig. 13 Analytical results with changing inner pressure summarized at each (a) inner pressure and (b) bending angle

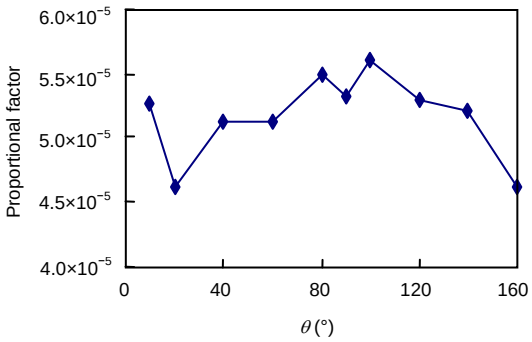

Fig. 14 Calculated proportional factors for k_1

from 10 to 50 mm. The results are plotted in Fig. 15a and Fig. 15b.

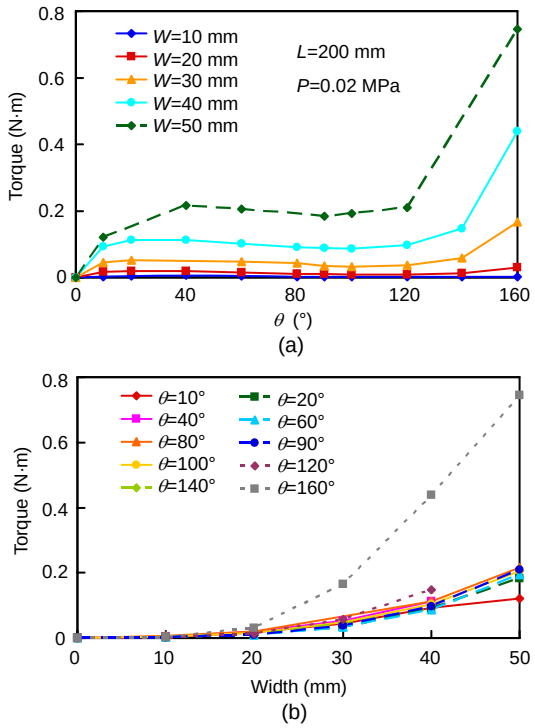

Fig. 15 Analytical results with changing width summarized as every (a) width and (b) bending angle

From these results, the torque is estimated to be in exponential proportion to width. In our former study, an effect factor of width seemed to be proportional to the third power of width under constant bending angle and inner pressure (Kimura *et al.*, 2006). Considering Eq. (1), the torque mainly depends on the volume change of the bag. Width is independent of length in this case because the torque is generated at the bending part. Total length of the bag has almost no influence on the torque. The volume of the bending part can be represented by the third power of width, w^3. Now, we obtain a proportional factor k_2 between the torque and w^3, where k_2 is a dimensionless value because k_2 is described by the after-mentioned Eq. (3).

The values in Fig. 15b are divided by w^3 and the criteria torque used on k_1. The average of k_2 is calculated, excluding the result of 10 mm width. The averaged k_2 values are summarized as illustrated in Fig. 16. The averaged k_2 values decrease slightly with bending angle. For the sake of simplicity, we determine k_2 as 1.6×10^4.

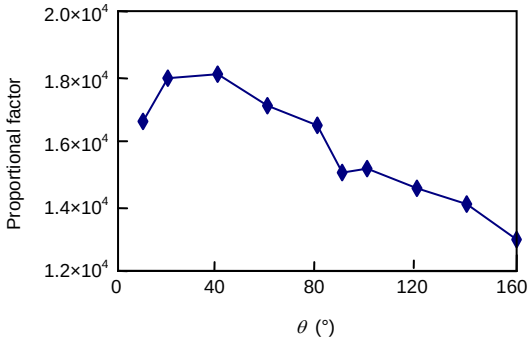

Fig. 16 Calculated proportional factors for k_2

Next, we examine the effect of bending angle θ for the torque. There are three torque generation modes. When bending angle is small, the torque shows the local maximum caused by local buckling. Around the range from 60° to 120°, the torque is almost constant. When the bending angle is large, the generated torque exponentially increases due to interference of face contact at the bending part. To obtain the torque dependency on bending angle, we apply a polynomial approximation to the criteria torque profile as follows:

$$\begin{aligned} T_s(\theta) = {} & 1.25\times10^{-10}\times\theta^5 - 4.74\times10^{-8}\times\theta^4 \\ & + 6.75\times10^{-6}\times\theta^3 - 4.42\times10^{-4}\times\theta^2 \\ & + 1.24\times10^{-2}\times\theta. \end{aligned} \tag{2}$$

Finally, we derive an empirical equation of the torque as follows:

$$T(p,w,\theta) = k_1 k_2 p w^3 T_s(\theta), \tag{3}$$

where k_1, k_2 and $T_s(\theta)$ are nondimensional quantities because pw^3 has the dimension of torque. The predictions of the empirical equation (the curved lines) and the analytical results (the plotted points) are shown in Fig. 17.

From these results, the observed torque agrees closely with the empirical equation. This equation contributes to the design of actuator bags.

3.3 Comparison between empirical equations and measurement values

To verify the empirical equation, comparison between the estimation and experimental results is necessary. The torque of actuator bags were measured by our original device as shown in Fig. 18.

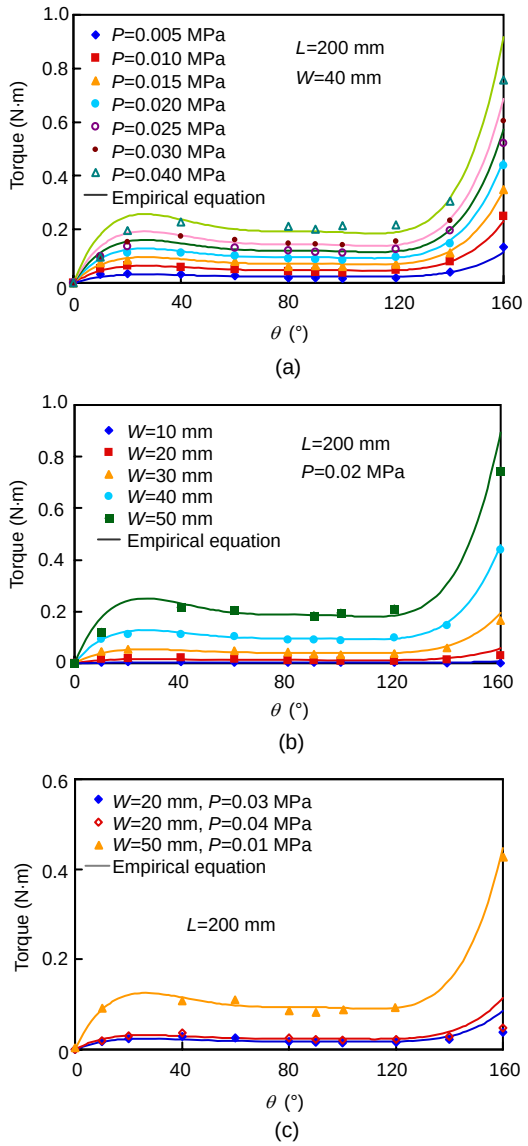

Fig. 17 Comparison between the empirical equation (the curved lines) and the analytical values (the plotted points) (a) about inner pressure, (b) about width and (c) at the conditions not used for the empirical equation

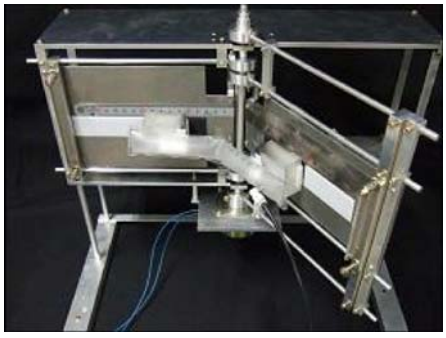

Fig. 18 Driving force measurement device

The specification of sample actuator bags is listed as follows: 100 mm in longitudinal length, 30 and 40 mm in width, 0.3 mm in urethane rubber thickness. Measurements were performed under 0.02 and 0.04 MPa for 30-mm width bag. And 0.02 MPa was applied to 40 mm. A deformation example is given in Fig. 19. Fig. 20 shows experimental results and estimations from the empirical equation.

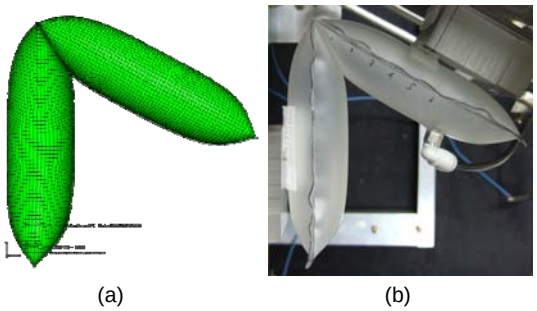

Fig. 19 Deformations of an actuator bag in (a) analysis and (b) measurement

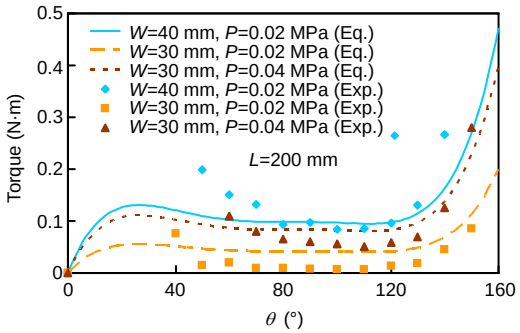

Fig. 20 Comparison between measurement values (Exp.) and the empirical equation (Eq.)

From these results, the measurement values agree with values from the empirical equation. This supports the validity of the empirical equation. The measurement values, however, are smaller than the estimated values at medium bending angles (about 70°–130°), and the measurement values are larger than the estimated values at small bending angles (under near 60°). The reason is assumed to be due to the torque loss in the measurement device. It is difficult to fix an actuator bag at a small bending angle. At a small bending angle, the bending position of an actuator bag is directed away from the axis of the measurement device. If the distance between the bending position and the axis increases, a longitudinal force of the actuator bag acts to open the device as

illustrated in Fig. 21. The device will require improvements to solve this problem.

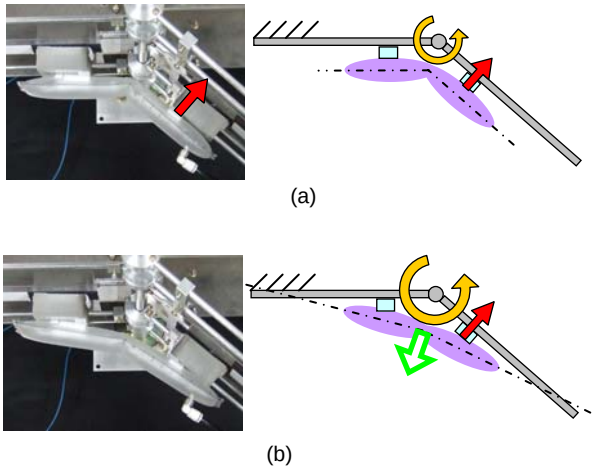

Fig. 21 Unexpected force acting on the driving force measurement device after an actuator bag has been directed away. (a) Deformation before being directed; (b) Deformation after being directed away

4 Conclusion

A new flexible mechanical system with a hydrostatic skeleton is proposed. The system consists of structural parts and actuator parts. By separating the roles, the required flow volume decreases, and higher efficiency is expected. A design guide for the structural part is discussed. For a convex shape, a highly elliptical shape decreases stress concentration. For a concave shape, the optimum fillet radius is obtained from the branch width of a cross shape. A T-shape is nearly the same.

The torque, as the driving force of the actuator part, is also discussed, dealing specifically with the large deformation of the bag. An empirical equation of the driving force is obtained by the nonlinear FEA. The equation can estimate the driving force from inner pressure, bag width and bending angle. This estimation is verified by experimental results, and the comparison supports the validity of the estimation equation.

There are three areas for future work. The first is further numerical study of a convex shape. The second is to estimate the torque dependency on material properties for various bag designs. The third is to improve the torque measurement device for small bending angle.

References

Hayakawa, Y., Pandian, S.R., 2005. Development of a Hybrid Element by using Sponge Core Soft Rubber Actuator. IEEE International Conference on Robotics and Automation, p.538-543. [doi:10.1109/ROBOT.2005.1570174]

Kimura, H., Kajimura, F., Maruyama, D., Koseki, M., Inou, N., 2006. Flexible Hermetically-sealed Mobile Robot for Narrow Spaces Using Hydrostatic Skeleton Driving Mechanism. IEEE/RSJ International Conference on Intelligent Robot and Systems, p.4006-4011. [doi:10.1109/IROS.2006.281840]

Kozulin, A.A., Skripnyak, V.A., 2004. Strength Calculation of Polymer Pipeline Elements. The 8th Russian-Korean International Symposium on Science and Technology KORUS, p.29-32. [doi:10.1109/KORUS.2004.1555661]

Ogden, R.W., 1972. Large deformation isotropic elasticity—on the correlation of theory and experiment for incompressible rubberlike solids. *The Royal Society of London, Series A, Mathematical and Physical Sciences*, **326**:565-584.

Ogden, R.W., 1997. Non-linear Elastic Deformations. Dover Publications, New York.

Pamplona, D.C., Goncalves, P.B., Lopes, S.R.X., 2006. Finite deformations of cylindrical membrane under internal pressure. *Journal of Mechanical Sciences*, **48**:683-696.

Suzumori, K., Abe, T., 1993. Applying a Flexible Microactuators to Pipeline Inspection Robots. International Symposium on Robotics and Manufacturing System IMACS/SICE, p.515-520.

Suzumori, K., Maeda, T., Watanabe, H., Hisada, T., 1997. Fiberless flexible microactuator designed by finite-element method. *IEEE/ASME Transactions on Mechatronics*, **2**(4):281-286. [doi:10.1109/3516.653052]